# Long-Horizon Direct Model Predictive Control for a Series-Connected Modular Rectifier

Mattia Rossi[1], Eyke Liegmann[2], Petros Karamanakos[3], Francesco Castelli-Dezza[1], Ralph Kennel[2]

[1] Politecnico di Milano, Milan, Italy
[2] Technical University of Munich, Munich, Germany
[3] Tampere University, Tampere, Finland

Corresponding author: Mattia Rossi, mattia.rossi@polimi.it
The Power Point Presentation will be made available after the conference

## Abstract

This paper presents a long-horizon direct model predictive control for a series-connected modular rectifier. The topology combines a diode rectifier and an active-front-end (AFE) converter to achieve a modular dc railway power supply. Two formulations of the optimization problem, i.e., power and current control, are investigated. The current control problem—solved with the sphere decoder for reduced computational effort—is compared with the power control problem—solved with exhaustive enumeration—in terms of current distortions and distribution of the harmonic spectrum. The latter have to meet strict grid standards, such as IEEE 519 and IEC 61000-2-4 standards. As shown, thanks to the long prediction horizon the total demand distortion of the converter current can be reduced, while keeping the device switching frequency low due to the medium voltage target.

## 1 Introduction

Electrified railway transportation systems are usually connected to high voltage (HV) ac grid, e.g., $132\,\mathrm{kV}$ or $150\,\mathrm{kV}$, through distributed traction power supplies, also called substations. They consist of a step-down transformer to achieve a medium voltage (MV) target and a conversion stage to provide ac or dc voltage to the feeder lines, with the latter being the focus of this paper. Whether it is the rail network throughput, or newly deployed trains, modern electrical railway networks present higher voltage drop along lines due to higher power requirements [1]. Since the standard substations are based on passive topologies, the increased power demand is commonly met either by expanding the existing infrastructure (which increases the investment cost), or by decreasing the speed of the trains to avoid unwanted trips of the feeder. However, since the peak demands vary in time, the additional rectifier capability may not be continuously needed. Hence, active-front-end (AFE) converter topologies are potential candidates to replace the currently used six- or twelve-pulse diode rectifiers (DR),since they introduce voltage controllability and bidirectional power flow while achieving a lower harmonic distortion due to the modulation principle.

In this paper, we consider the Italian regional railway network at $3\,\mathrm{kV}$ as a case study. The rated dc-link voltage level of the overhead lines is set to $3.6\,\mathrm{kV}$. The terminals of the substations are subject to significant dc-link fluctuations due to power fluctuations [2]. Note, however, that the power gradients may happen for short time, thus, the controllability range might be limited. For this reason, the topology proposed in [3] is considered in this work. According to this topology, a DR is connected in series with an AFE converter to introduce voltage controllability against dc-link voltage fluctuations, redundancy—and thus higher reliability—with respect to the output dc voltage, and power/voltage scalability, while keeping the cost-effective benefit of DRs that relates to the cost of a substation upgrade. Thus, such a solution allows for longer distance between substations, reduced losses in rolling stock (e.g., without dissipating energy via brake resistors to balance the dc link) and even prevention of interruptions caused by an undervoltage trip. Finally, considering the chosen case study, it should be mentioned that both modules are connected via a dual-winding transformer to the point of common coupling (PCC), which acts as the connection point of the conversion system to the HV grid. In addition, $L$-filters are employed to reduce current and voltage harmonics at the PCCs since tight standards are imposed at this point, see, e.g., the IEEE 519 [4] and IEC 61000-2-4 [5].

As mentioned above, the chosen topology enables controllability of the dc voltage by manipulating the power demand from the ac grid. To this aim, model predictive control (MPC) can be employed, since it has been shown to be a promising alternative to conventional control methods [6], [7]. More specifically, in this work, direct MPC, also called finite control set MPC (FCS-MPC)—i.e., MPC where the control and modulation take place in one computational stage—is employed for the inner loop of a

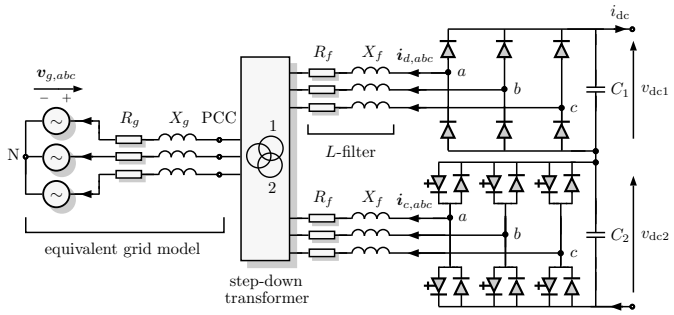


**Fig. 1:** Grid-tied series-connected modular rectifier based a DR and a AFE converter, with $L$ input filters.

**Tab. 1:** System parameters for a $3\,\mathrm{kV}$ dc feeder

| | | |
|---|---|---|
| input voltage | $V_R$ | $1.2\,\mathrm{kV}$ |
| input current | $I_R$ | $833\,\mathrm{A}$ |
| apparent power | $S_R$ | $1.73\,\mathrm{MVA}$ |
| grid frequency | $f_g$ | $50\,\mathrm{Hz}$ |
| dc-link voltage | $V_{\rm dc}$ | $3.6\,\mathrm{kV}$ |
| dc-link current | $I_{\rm dc}$ | $718\,\mathrm{A}$ |
| grid inductance | $L_g$ | $0.128\,\mathrm{mH}$ |
| grid resistance | $R_g$ | $3.02\,\mathrm{m\Omega}$ |
| leakage inductance | $L_t$ | $0.77\,\mathrm{mH}$ |
| leakage resistance | $R_t$ | $5.1\,\mathrm{m\Omega}$ |
| filter inductance | $L_f$ | $1.1\,\mathrm{mH}$ |
| filter resistance | $R_f$ | $4\,\mathrm{m\Omega}$ |
| short-circuit ratio | $k_{sc}$ | $20.64$ |

cascaded control structure as in [3]. For the latter, two different formulations are discussed, i.e., a power and a current control problem are formulated in the framework of FCS-MPC. As for the outer loop, it regulates the dc-link voltage of the AFE converter along a desired value computed by discarding the DR voltage contribution from the requested voltage on the dc side.

Although several direct MPC-based strategies for both power [8], [9] and current control [10] of a grid-tied two-level converter have been proposed, this paper discusses their performances in terms of grid current total demand distortion (TDD). As shown, even if both approaches use similar prediction models, current MPC achieves a better harmonic distribution, which helps to meet the grid standards. This is also facilitated by the implementation of longer prediction horizons, that are commonly employed to improve the system performance [11], [12]. More specifically, as discussed in the paper, for the current control problem, owing to its linear nature, a dedicated branch-and-bound algorithm, known as sphere decoder, is adopted [13]. Thanks to the effective pruning of suboptimal options, the computational complexity of the problem can be kept modest. On the other hand, the nonlinearities that arise during the formulation of the power control problem do not allow for such a solution. Thus, the brute force approach of exhaustive search is used, implying that a relatively long horizon can lead to a computationally intractable problem.

Both control approaches are compared in terms of grid current distortions, while the corresponding harmonic spectra are assessed with respect to the IEEE 519 and IEC 61000-2-4 standards. It is noteworthy that both MPC approaches implement explicit output (hard) constraints to deal with the inherent limitation of the system controllability. By doing so, the minimum condition which ensures that the AFE converter does not enter six-pulse operation is always met.

## 2 Case Study: Traction Power Supply at 3kV

The modular rectifier used in this work comprises of a six-pulse DR and a two-level AFE converter as shown in Fig. 1. The modules share the same dc current $i_{\rm dc}$, which is imposed by the load. The total dc-link voltage is $v_{\rm dc}(t) = v_{\rm dc1}(t) + v_{\rm dc2}(t)$, where $v_{\rm dc1}(t)$ refers to the (fixed) DR contribution, while $v_{\rm dc2}(t)$ is the controllable variable. A disadvantage of such a connection is that semiconductor devices with a higher reverse blocking voltage and higher insulation may be needed since they must sustain the full dc-link current.

The modules are connected to the grid via a step-down transformer. To simplify the analysis, equal secondary windings are assumed. Nevertheless, since the DR and the AFE converter generate different harmonics at the PCC, i.e., the DR produces higher distortions due to its uncontrolled nature, the secondary windings could be differentiated instead. Note that the ac grid might not permit energy recuperation at the PCC due to grid-stability concerns. In such a case, off-board energy storage devices can be used [2]. The latter should not be considered just an alternative to the upgrade of standard substations, but a viable extension to increase the rail system scalability that will enable, e.g., the integration of renewable energy sources.

## 3 Controller Model

In the sequel, a mathematical description of the converter dynamics is derived in the $\alpha\beta$-reference frame. All variables given in the $abc$-plane $\boldsymbol{\xi}_{abc} = [\xi_a\ \xi_b\ \xi_c]^T$ are mapped into two-dimensional vectors $\boldsymbol{\xi}_{\alpha\beta} = [\xi_\alpha\ \xi_\beta]^T$ via the Clarke transformation matrix $\boldsymbol{K}$ (without the common-mode component)

$$\boldsymbol{K} = \frac{2}{3}\begin{bmatrix} 1 & -\frac{1}{2} & -\frac{1}{2} \\ 0 & \frac{\sqrt{3}}{2} & -\frac{\sqrt{3}}{2} \end{bmatrix} \tag{1}$$

Hereafter, to simplify the notation, the subscript $\alpha\beta$ is dropped from all vectors, unless otherwise stated. Moreover, $\boldsymbol{\xi}_{\alpha\beta}$ can be mapped into a variable $\boldsymbol{\xi}_{dq} = [\xi_d\ \xi_q]^T$ in the rotating $dq$-reference frame, by applying $\boldsymbol{R}(\varphi_g)$, i.e., $\boldsymbol{\xi}_{dq} = \boldsymbol{R}(\varphi_g)\boldsymbol{\xi}_{\alpha\beta}$ with

$$\boldsymbol{R}(\varphi_g) = \begin{bmatrix} \cos(\varphi_g) & \sin(\varphi_g) \\ -\sin(\varphi_g) & \cos(\varphi_g) \end{bmatrix} \tag{2}$$

which depends on the phase angle $\varphi_g$, to be selected according to desired $dq$-orientations. Finally, throughout

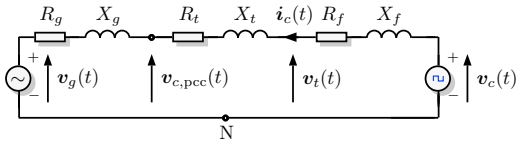


**Fig. 2:** Equivalent circuit of the AFE converter side in the $\alpha\beta$-plane. The PCC is denoted by the voltage $\boldsymbol{v}_{c,\mathrm{pcc}}(t)$.

the paper, all SI variables are normalized based on the rated values of the step-down transformer[1].

Consider the grid voltage $\boldsymbol{v}_g(t)$ as shown in Fig. 1. The distribution lines are approximated by the grid resistance $R_g$ and reactance $X_g$ (computed from the inductance as $\omega_g L_g$). Likewise, the step-down transformer can be represented by its series resistance $R_t$ and leakage reactance $X_t$, while the $L$ filter by the reactance $X_f$ and its internal resistor $R_f$. All resistances and reactances are lumped into the equivalent quantities $R = R_g + R_t + R_f$ and $X = X_g + X_t + X_f$. To the right of PCC, we define the input current $\boldsymbol{i}_c(t)$ and voltage $\boldsymbol{v}_c(t)$ of the AFE converter, while $\boldsymbol{i}_d(t)$ and $\boldsymbol{v}_d(t)$ refer to the corresponding quantities of the DR. Currents flowing towards the grid are assumed to be positive.

## 3.1 Physical Model of the Grid

Assuming a balanced three-phase grid, it can be modeled in the $\alpha\beta$-plane as $\boldsymbol{v}_g = [V_g \cos(\omega t)\ V_g \sin(\omega t)]^T$. Hence, the instantaneous grid voltage variations are described by

$$\frac{\mathrm{d}\boldsymbol{v}_g(t)}{\mathrm{d}t} = \omega_g \begin{bmatrix} 0 & -1 \\ 1 & 0 \end{bmatrix} \boldsymbol{v}_g(t) \tag{3}$$

The secondary side of the transformer is characterized by the real $P_{\mathrm{in}x}$, reactive $Q_{\mathrm{in}x}$, and apparent $S_{\mathrm{in}x}$ powers, where $x \in \{1, 2\}$ denotes the power of the DR ($x = 1$) or the AFE converter ($x = 2$), see Fig. 1. For the latter, the power factor is $\mathrm{pf} = |\cos(\phi)| = P_{\mathrm{in}2}/S_{\mathrm{in}2}$, where $\phi$ is the phase angle between $\boldsymbol{v}_t(t)$ and $\boldsymbol{i}_c(t)$ waveforms.

## 3.2 Physical Model of the AFE Converter

Given the equivalent circuit in Fig. 2, the ac side dynamics are described in the $\alpha\beta$-plane as

$$X\frac{\mathrm{d}\boldsymbol{i}_c(t)}{\mathrm{dt}} = -R\boldsymbol{i}_c(t) - \boldsymbol{v}_g(t) + \boldsymbol{v}_c(t) \tag{4}$$

where the AFE converter voltage $\boldsymbol{v}_c$ is determined by the three-phase switch position $\boldsymbol{u}_{abc} = [u_a\, u_b\, u_c]^T \in \boldsymbol{\mathcal{U}} = \mathcal{U}^3$, with $u_a, u_b, u_c \in \mathcal{U} = \{-1, 1\}$, and the dc-link voltage $V_{\mathrm{dc}2}$, i.e.,

$$\boldsymbol{v}_c(t) = V_{\mathrm{dc}2}\boldsymbol{K}\boldsymbol{u}_{abc}(t) = V_{\mathrm{dc}2}\boldsymbol{u}(t) \tag{5}$$

[1] According to Table 1, the per unit (p.u.) system is established based on the base quantities $V_B = \sqrt{2/3}V_R$, $I_B = \sqrt{2}I_R$, $S_B = S_R = (3/2)\,V_B I_B$, and $\omega_B = \omega_g = 2\pi f_g$, where $V_R$ and $I_R$ denote the (rated) rms line-to-line voltage and rms line current referred to the secondary side of the transformer.

Given the definition of $\mathcal{U}$, it can be deduced that there are $2^3 = 8$ three-phase switch position combinations.

The controller model used by the MPC algorithm formulated as current controller, predicts the evolution of the converter input currents in the $\alpha\beta$-plane. By defining the state vector $\boldsymbol{x}(t) = \left[\boldsymbol{i}_c^T(t)\ \boldsymbol{v}_g^T(t)\right]^T \in \mathbb{R}^4$, the output vector $\boldsymbol{y}(t) = \boldsymbol{i}_c(t) \in \mathbb{R}^2$, and the three-phase switch position $\boldsymbol{u}_{abc}(t)$ as the input to the system, the continuous-time state-space representation is

$$\frac{\mathrm{d}\boldsymbol{x}(t)}{\mathrm{d}t} = \boldsymbol{F}\boldsymbol{x}(t) + \boldsymbol{G}\boldsymbol{u}_{abc}((t) \tag{6}$$

$$\boldsymbol{y}(t) = \boldsymbol{C}\boldsymbol{x}(t) \tag{7}$$

where matrices $\boldsymbol{F} \in \mathbb{R}^{4\times4}$, $\boldsymbol{G} \in \mathbb{R}^{4\times2}$, and $\boldsymbol{C} \in \mathbb{R}^{4\times4}$ are

$$\boldsymbol{F} = \begin{bmatrix} -\frac{R}{X}\boldsymbol{I}_2 & -\frac{1}{X}\boldsymbol{I}_2 \\ \boldsymbol{0}_{2\times2} & \omega_g \begin{bmatrix} 0 & -1 \\ 1 & 0 \end{bmatrix} \end{bmatrix} \tag{8}$$

$$\boldsymbol{G} = \begin{bmatrix} \frac{1}{X}\boldsymbol{I}_2 & \boldsymbol{0}_{2\times2} \end{bmatrix}^T V_{\mathrm{dc}2}\boldsymbol{K} \tag{9}$$

$$\boldsymbol{C} = \begin{bmatrix} \boldsymbol{I}_2 & \boldsymbol{0}_{2\times2} \end{bmatrix} \tag{10}$$

The controller model used by the second MPC algorithm, i.e., power control problem, predicts the evolution of the real and reactive powers in the $\alpha\beta$-plane. From the instantaneous power theory, it follows that[2]

$$P_{\mathrm{in}2}(t) = v_{g\alpha}(t)i_{c\alpha}(t) + v_{g\beta}(t)i_{c\beta}(t) \tag{11}$$

$$Q_{\mathrm{in}2}(t) = v_{g\alpha}(t)i_{c\beta}(t) - v_{g\beta}(t)i_{c\alpha}(t) \tag{12}$$

For the sake of simplicity, $P_{\mathrm{in}2}(t)$ and $Q_{\mathrm{in}2}(t)$ refer to the grid voltage source instead of the PCC. By defining the output vector $\boldsymbol{y}(t) = [P_{\mathrm{in}2}(t)\ Q_{\mathrm{in}2}(t)]^T \in \mathbb{R}^2$ it follows that

$$\boldsymbol{y}(t) = \boldsymbol{h}\left(\boldsymbol{x}(t)\right) \tag{13}$$

where $\boldsymbol{h}(\boldsymbol{x}(t)) \in \mathbb{R}^2$ is

$$\boldsymbol{h}(\boldsymbol{x}(t)) = \begin{bmatrix} x_1(t)x_3(t) + x_2(t)x_4(t) \\ x_2(t)x_3(t) - x_1(t)x_4(t) \end{bmatrix} \tag{14}$$

As can be seen, the system output (13) used for the power controller is a nonlinear combination of the state.

MPC requires the prediction model of the system to be in the discrete-time domain. Since $\boldsymbol{F}$ and $\boldsymbol{G}$ are assumed to be time-invariant matrices, the system dynamics, given by (6) are discretized by using exact discretization[3] with the sampling interval $T_s$. This yields

$$\boldsymbol{x}(k+1) = \boldsymbol{A}\boldsymbol{x}(k) + \boldsymbol{B}\boldsymbol{u}_{abc}(k) \tag{15}$$

$$\boldsymbol{y}(k) = \begin{cases} \boldsymbol{C}\boldsymbol{x}(k) & \text{from (7)} \\ \boldsymbol{h}\left(\boldsymbol{x}(k)\right) & \text{from (13)} \end{cases} \tag{16}$$

[2] Note that, due to the adoption of the p.u. system the factor $3/2$ is neglected from (11) and (12).

[3] Since an ideal grid is assumed, the amplitude $V_g$ and frequency $\omega_g$ of $\boldsymbol{v}_g$ are constant. This implies that $\boldsymbol{F}$ is time invariant. Nevertheless, if the grid is subject to voltage/current imbalances, $\boldsymbol{v}_g$ may be considered as an external disturbance instead of a state which allows for $\boldsymbol{F}$ to remain time invariant.

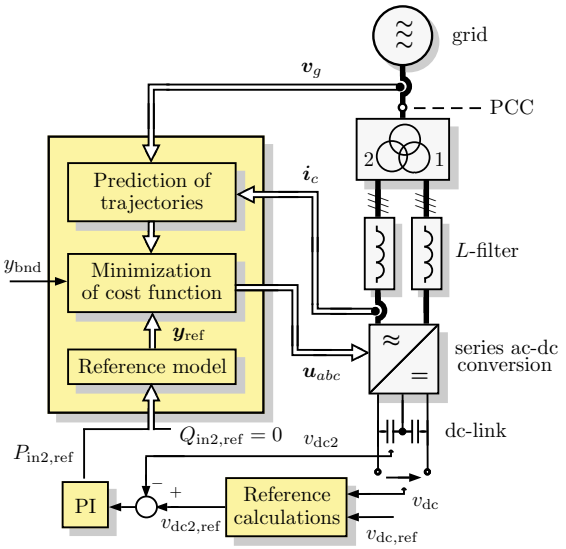


**Fig. 3:** Direct MPC with reference tracking for the series ac-dc conversion system shown in Fig. 1, where the reference model block returns $\boldsymbol{y}_{\rm ref}(t) = [P_{\rm in2,ref}(t)\ Q_{\rm in2,ref}(t)]^T$ or $\boldsymbol{y}_{\rm ref}(t) = [i_{cd,\rm ref}(t)\ i_{cq,\rm ref}(t)]^T$.

with $\boldsymbol{A} = \mathbf{e}^{\boldsymbol{F}T_s}$ and $\boldsymbol{B} = -\boldsymbol{F}^{-1}(\boldsymbol{I}_4 - \boldsymbol{A})\,\boldsymbol{G}$. $\boldsymbol{I}_4$ is the four-dimensional identity matrix, $\mathbf{e}$ the matrix exponential, and $k \in \mathbb{N}$ denotes the discrete-time step. To keep a simple notation, the output $\boldsymbol{y}(k)$ from the compact form (16) is assumed in the remainder of the paper.

# 4 Long-Horizon Direct MPC with References Tracking

The proposed direct model predictive control approaches aim to regulate the converter currents or the real and reactive power along their reference values. Such objectives should be met while both operating the converter at a low switching frequency for reduced switching losses, and meeting the grid codes. The complete block diagram of the proposed algorithm is depicted in Fig. 3.

To derive the desired reference values for both MPC controllers, the total dc-link voltage $v_{\rm dc}(t)$ needs to be controlled. This is done via $v_{\rm dc2}(t)$, the reference of which $v_{\rm dc2,ref}(t)$ is computed based on the estimation of $v_{\rm dc1}(t)$, as in [3]. Following, the phase angle $\varphi_g = \int_0^{T_s} \omega_g\,{\rm d}t$ calculated through a phase-locked-loop (PLL) algorithm is used to perform the transformation from the stationary to the rotating plane. In doing so, the power components in (11) and (12), can be rewritten as

$$P_{\rm in2}(t) = \frac{3}{2}\left(v_{gd}(t)i_{cd}(t) + v_{gq}(t)i_{cq}(t)\right) \tag{17}$$

$$Q_{\rm in2}(t) = \frac{3}{2}\left(v_{gd}(t)i_{cq}(t) + v_{gq}(t)i_{cd}(t)\right) \tag{18}$$

By aligning the $d$-axis with the grid voltage, the $q$-component of $\boldsymbol{v}_{g,dq}(t)$ becomes zero, which further simplifies the power expressions to

$$P_{\rm in2}(t) = \frac{3}{2}v_{gd}(t)i_{cd}(t) \iff i_{cd}(t) = \frac{2}{3}\frac{P_{\rm in2}(t)}{v_{gd}(t)} \tag{19}$$

$$Q_{\rm in2}(t) = \frac{3}{2}v_{gd}(t)i_{cq}(t) \iff i_{cq}(t) = \frac{2}{3}\frac{Q_{\rm in2}(t)}{v_{gd}(t)} \tag{20}$$

Thanks to the above equations, both MPC schemes can utilize the same outer voltage loop, which provides the reference value for the real power $P_{\rm in2,ref}(t)$ while the reactive one $Q_{\rm in2,ref}(t)$ is set to zero to achieve ${\rm pf} = 1$. According to the controller type, $\boldsymbol{y}_{\rm ref}(t)$ refers to power or current references derived from (19) and (20).

## 4.1 Reference Calculations and Controllability Constraints

Since $i_{\rm dc}$ is constant, the DR is assumed to be operating at rated operating conditions. By considering the voltage drop on the equivalent reactance $X$ and resistance $R$, the average dc voltage at rated operating conditions can be easily computed with

$$\widehat{V}_{\rm dc1} = \frac{3}{\pi}\left(\sqrt{2}V_R - (R+X)\,i_{\rm dc}\right) \tag{21}$$

All intermediate steps which lead to (21) are described in [14]. Given the total dc-link voltage reference $v_{\rm dc,ref}(t)$, it follows that $v_{\rm dc2,ref}(t) = v_{\rm dc,ref}(t) - \widehat{V}_{\rm dc1}$.

However, the system controllability is limited. If the input power of the AFE converter is lower than a minimum value $P_{\rm in2,min}$, then it enters six-steps operation, behaving as a DR. The corresponding minimum dc-link voltage value $V_{\rm dc2,min}$ is computed similarly to (21). Given that both MPC algorithms aim to operate the system with ${\rm pf} = 1$, i.e., the dc-link power is equal to the real power $P_{\rm in2}(k) = S_{\rm in2}(k) = P_{\rm dc2}(k)$, it follows that $P_{\rm in2,min} = V_{\rm dc2,min}i_{\rm dc}$. Likewise, the minimum value for the current has to be $i_{c,\rm min} = (2/3)P_{\rm in2,min}/v_{gd}(k)$, where $v_{gd}(k)$ at steady-state is constant and equal to one for nominal operation.

Based on the above analysis, the relevant lower bound is added to the optimization problem in the form of the following (hard) explicit output constraint

$$||\boldsymbol{y}(k+1)||^2_{\boldsymbol{M}} \geq y^2_{\rm bnd} \tag{22}$$

where the scalar $y_{\rm bnd}$ and the matrix $\boldsymbol{M}$ depend on the control problem, i.e. $y_{\rm bnd} > P_{\rm in2,min} \in \mathbb{R}^+$ and $\boldsymbol{M} = {\rm diag}(1,0)$ or $y_{\rm bnd} > i_{c,\rm min} \in \mathbb{R}^+$ and $\boldsymbol{M} = {\rm diag}(1,1)$, respectively. With the inclusion of such a constraint MPC guarantees that the AFE converter is controllable over the entire operating regime.

## 4.2 Optimization Problem Formulation

As mentioned at the beginning of this section, both MPC algorithms aim to regulate the output vector along its reference $\boldsymbol{y}_{\rm ref}$ while operating the system at a low switching frequency $f_{\rm sw}$, with the goal to fulfill the grid standards limits given in terms of TDD.

Given a prediction horizon of $N_p$ steps, the aforementioned control objectives at time step $k$ are mapped into a scalar through the generalized cost function[4]

$$J(k) = \sum_{\ell=k}^{k+N_p-1} ||\boldsymbol{y}_{\text{ref}}(\ell+1) - \boldsymbol{y}(\ell+1)||^2_{\boldsymbol{Q}} + \lambda_u ||\Delta \boldsymbol{u}_{abc}(\ell)||_1 \tag{23}$$

where $J(k) : \mathbb{R}^2 \times \boldsymbol{\mathcal{U}} \rightarrow \mathbb{R}^+$. The entries of the weighting matrix $\boldsymbol{Q}$ penalize the output tracking performance of MPC. For the MPC-based power controller we set $\boldsymbol{Q} = \boldsymbol{Q_q} = \text{diag}\left((1-\lambda_q), \lambda_q\right) \in \mathbb{R}^{2\times 2}$, whereas $\boldsymbol{Q} = \boldsymbol{Q_c} = \boldsymbol{I}_2 \in \mathbb{R}^{2\times 2}$ for the current controller, with $\boldsymbol{Q_q} \neq \boldsymbol{Q_c}$. By adjusting $\lambda_q$, e.g., $\lambda_q < 0.5$, the tracking of $P_{\text{in2}}(k+1)$ is prioritized. The term $\Delta \boldsymbol{u}_{abc}(k)$ penalizes the switching effort defined as the difference between two consecutive switch positions, i.e., $\Delta \boldsymbol{u}_{abc}(k) = \boldsymbol{u}_{abc}(k) - \boldsymbol{u}_{abc}(k-1)$.[5] The latter directly relates to the device (average) switching frequency [16]. Hence, The weighting factors $\lambda_q, \lambda_u \in \mathbb{R}^+$ decide on the tradeoff between the tracking accuracy of the controller and the switching effort. By using the p.u. system, the real and reactive power values are of the same magnitude, thus $\lambda_q \in [0, 1]$, while $\lambda_u > 0$ is chosen such that a low $f_{\text{sw}}$ results. The output reference $\boldsymbol{y}_{\text{ref}}(k+1)$ is computed through the reference model block given in Fig. 3.

Then, to find the optimal sequence of control actions $\boldsymbol{U}^*_{abc}(k) = \left[\boldsymbol{u}^{*T}_{abc}(k)\ \boldsymbol{u}^{*T}_{abc}(k+1)\ \ldots\ \boldsymbol{u}^{*T}_{abc}(k+N_p-1)\right]^T$, the following integer optimization problem needs to be solved in real time

$$\boldsymbol{U}^*_{abc}(k) = \arg \underset{\boldsymbol{U}_{abc}(k)}{\text{minimize}}\ J(k) \tag{24}$$

$$\text{subject to } \boldsymbol{x}(\ell+1) = \boldsymbol{A}\boldsymbol{x}(\ell) + \boldsymbol{B}\boldsymbol{u}_{abc}(\ell) \tag{25}$$

$$\boldsymbol{y}(\ell+1) = \begin{cases} \boldsymbol{C}\boldsymbol{x}(\ell+1) \\ \boldsymbol{h}\left(\boldsymbol{x}(\ell+1)\right) \end{cases} \tag{26}$$

$$||\boldsymbol{y}(\ell+1)||^2_{\boldsymbol{M}} \geq y^2_{\text{bnd}} \tag{27}$$

$$\forall \ell = k, ..., k+N_p-1$$

$$\boldsymbol{U}_{abc}(k) \in \mathbb{U} \tag{28}$$

where the optimization variable is the sequence of three-phase switch positions over the horizon, i.e., $\boldsymbol{U}_{abc}(k) = \left[\boldsymbol{u}^T_{abc}(k)\ \boldsymbol{u}^T_{abc}(k+1)\ \ldots\ \boldsymbol{u}^T_{abc}(k+N_p-1)\right]^T \in \mathbb{U}$, with $\mathbb{U} \in \boldsymbol{\mathcal{U}}^{N_p} \subset \mathbb{Z}^{3N_p}$ being the feasible set. Out of the optimal control sequence $\boldsymbol{U}^*_{abc}(k)$ only the action at time step $k$, i.e., $\boldsymbol{u}^*_{abc}(k)$, is applied, whereas all the remaining elements are discarded. Then, the optimization is repeated over a shifted horizon by one time step based on new measurements and/or estimates, according to the receding horizon principle.

[4] Note that $||\boldsymbol{\xi}||^2_{\boldsymbol{Q}} = \boldsymbol{\xi}^T\boldsymbol{Q}\boldsymbol{\xi}$ denotes the squared norm of the vector $\boldsymbol{\xi}$ weighted with the positive definite matrix $\boldsymbol{Q}$.

[5] Note that the use of $\ell_1$- or $\ell_2$-norm does not make any difference since $\Delta \boldsymbol{u}_{abc}(k) \in \{-1, 0, 1\}$ [15].

## 4.3 Solving the Optimization Problem

A straightforward approach to solve (24) is by *enumerating* all feasible $\boldsymbol{u}_{abc}(k)$ and choosing the one which results in the minimum value of $J(k)$. This implies that number of candidate solutions increases exponentially with the length of the horizon, i.e., $2^{3N_p}$ possible switch combinations need to be taken into account [17].

An interesting attribute of the current MPC problem formulation is the linear mapping of the system state to the controlled output, see (7). This, along with the linear model of the system (6) and the quadratic cost function (23), allows for reformulation of the optimization problem, as detailed in [13], [18]. As shown, by applying some algebraic manipulations, the problem can be written as a truncated integer least-squares (ILS) problem in a vector form. In doing so, effective optimizers, such as a sphere decoding algorithm [19], that keep the pronounced computational complexity at bay can be employed.

Specifically, it can be shown that by relaxing the feasible set of the optimization problem from $\mathbb{U}$ to $\mathbb{R}^n$, with $n = 3N_p$, the unconstrained solution $\boldsymbol{U}_{\text{unc}}(k)$ can be computed. With that, the MPC current control problem can be written as

$$\boldsymbol{U}^*_{abc}(k) = \arg \underset{\boldsymbol{U}_{abc}(k)}{\text{minimize}}\ ||\bar{\boldsymbol{U}}_{\text{unc}}(k) - \boldsymbol{V}\boldsymbol{U}_{abc}(k)||^2_2 \tag{29}$$

$$\text{subject to } \boldsymbol{U}_{abc}(k) \in \mathbb{U} \tag{30}$$

$$\forall \ell = k, ..., k+N_p-1$$

where $\bar{\boldsymbol{U}}_{\text{unc}}(k) = \boldsymbol{V}\boldsymbol{U}_{\text{unc}}(k)$. The nonsingular lower triangular matrix $\boldsymbol{V} \in \mathbb{R}^{3N\times 3N}$ is known as the lattice generator matrix, and it depends on the system matrices, the sequence of reference values over the horizon, the current state $\boldsymbol{x}(k)$, and the previously applied switch position $\boldsymbol{u}^*_{abc}(k-1)$; see [13].

To find the integer solution $\boldsymbol{U}^*_{abc}(k)$ of (29) a sphere decoder is implemented in line [13]. It is important to mention that this solution—which represents the lattice point with the shortest Euclidean distance to $\bar{\boldsymbol{U}}_{\text{unc}}(k)$—is the same solution as that of the original problem. Therefore, even though $\boldsymbol{U}^*_{abc}(k)$ can be found much faster with the sphere decoder, its optimality is still guaranteed. For more details on the design, analysis and implementation of sphere decoder the interested reader is referred to [13], [20], [21].

On the other hand, the power control problem cannot be reformulated as an ILS one. This is due to the nonlinear relationship between the state and the output, see (13). As a result, the exhaustive enumeration is adopted for this problem, implying that the length of the prediction horizon should be limited to a few steps to keep the computational load manageable. This implies that the performance benefits associated with long prediction

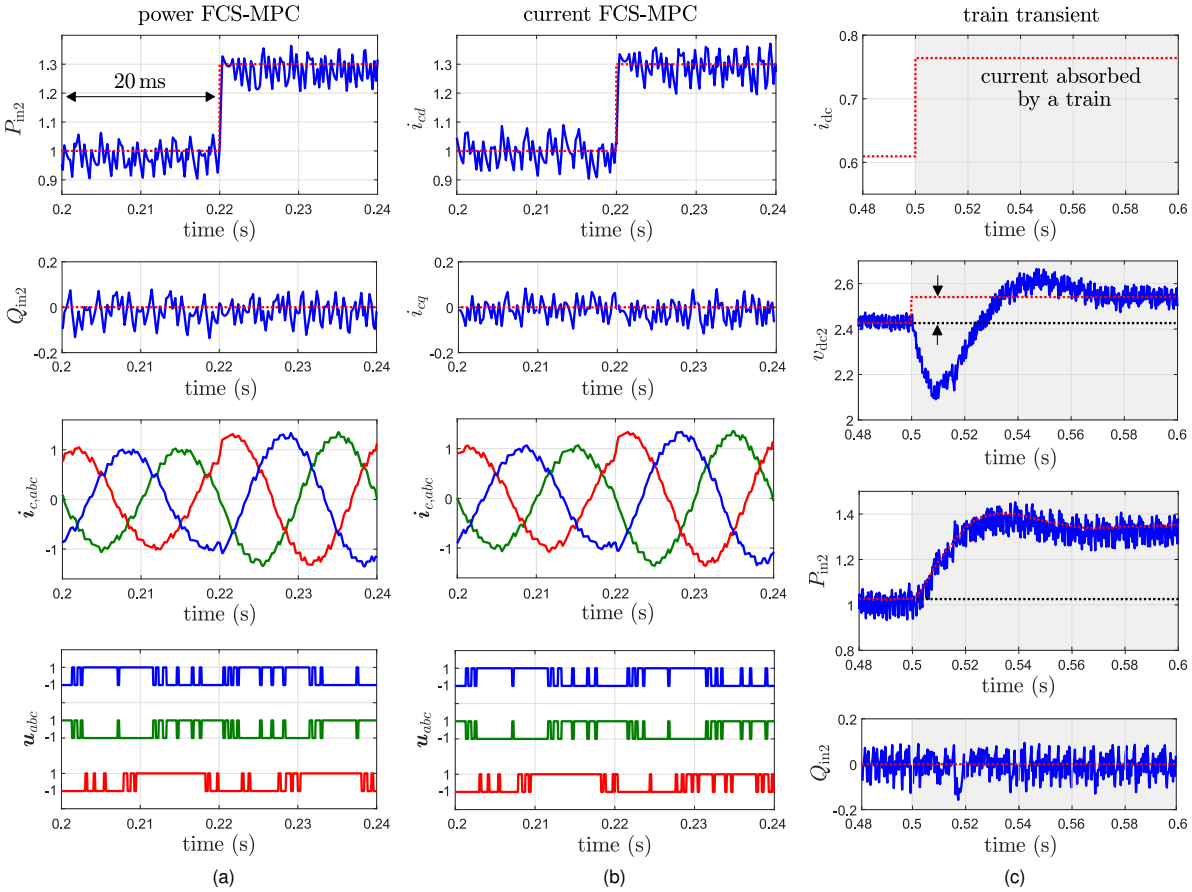


**Fig. 4:** Simulated waveforms for steady-state operation and two transient scenarios. (a) Power FCS-MPC: real and reactive power (blue lines) and their references (red dotted lines), three-phase currents, and switch positions. (b) Current FCS-MPC: converter currents in the $dq$-reference frame (blue lines) and their references (red dotted lines), three-phase waveforms, and switch positions. (c) Train transient: dc current absorbed by a train, stabilization of $v_{\mathrm{dc}}(t)$ through $v_{\mathrm{dc2}}(t)$ (blue lines) and its reference (red dotted lines), real and reactive power (blue lines) and their references (red dotted lines), note that such waveforms may be achivied either by power FCS-MPC as well as current FCS-MPC.

horizons cannot be harvested by the power controller, as also verified in Section 5.

# 5 Simulations Results

Given the system in Fig. 3, the performance of both MPC algorithms is evaluated through MATLAB simulations, with a sampling interval $T_s = 50\,\mu\mathrm{s}$. The system parameters are given in Table 1. The design of the outer controller—based on proportional-integral (PI) controllers—is out of the scope of the paper, and thus not discussed. The voltage at the PCC is computed based on the equivalent circuit shown in Fig. 2. All results are presented in the p.u. system.

## 5.1 Steady-State Operations

The steady-state performance of the system is evaluated within one period $T_g = 1/f_g = 20\,\mathrm{ms}$, which is highlighted in Fig. 4 (from $0.2$ to $0.22\,\mathrm{s}$). In particular, the simulation results shown in Fig. 4(a) refer to the power FCS-MPC, while Fig. 4(b) to the current FCS-MPC. For both controllers, the chosen prediction horizon is $N_p = 4$ while $\lambda_u$ is tuned to achieve the same switching frequency, i.e., $f_{\mathrm{sw}} \approx 450\,\mathrm{Hz}$. Moreover, $\lambda_q = 0.4$ to prioritize the real power tracking. The real and reactive power (blue line) accurately track their references (red dotted lines). Likewise, good tracking performance is achieved by the AFE converter currents. The three-phase switch positions are shown at bottom of the respective figures. Since in both cases $Q_{\mathrm{in2}}(t) \approx 0$ is achieved, the real power $P_{\mathrm{in2}}(t)$ equals the apparent power $S_R = 1\,\mathrm{p.u.}$ ($\mathrm{pf} = 1$), thus, the total dc-link power is $P_{\mathrm{dc}}(t) = P_{\mathrm{in1}}(t) + S_R$, where $P_{\mathrm{in1}}(t) < S_R$ since $\mathrm{pf} \neq 1$ holds for the DR [3]. Note that, the different power tracking may presents an offset with respect to their references as side effect of MPC, which does not include a proper integral; the latter is included in the voltage controller, achieving zero steady-state error, see Fig. 4(c).

The performances on the ac side are assessed in terms of current TDD $I_{c,\mathrm{TDD}}(\%)$, voltage TDD $V_{c,\mathrm{TDD}}(\%)$, and harmonic content distribution. Therefore, Figs. 5(a) and 5(c) show the voltages at the PCC $\boldsymbol{v}_{c,\mathrm{pcc},abc}(t)$ while 5(b) and 5(d) the currents $\boldsymbol{i}_{c,abc}(t)$, respectively, along with their corresponding harmonic spectra. Due to the absence of a modulator and the consequent variable $f_{\mathrm{sw}}$, both MPC-based controllers have nondeterministic spectra, with the energy being distributed over a wide range

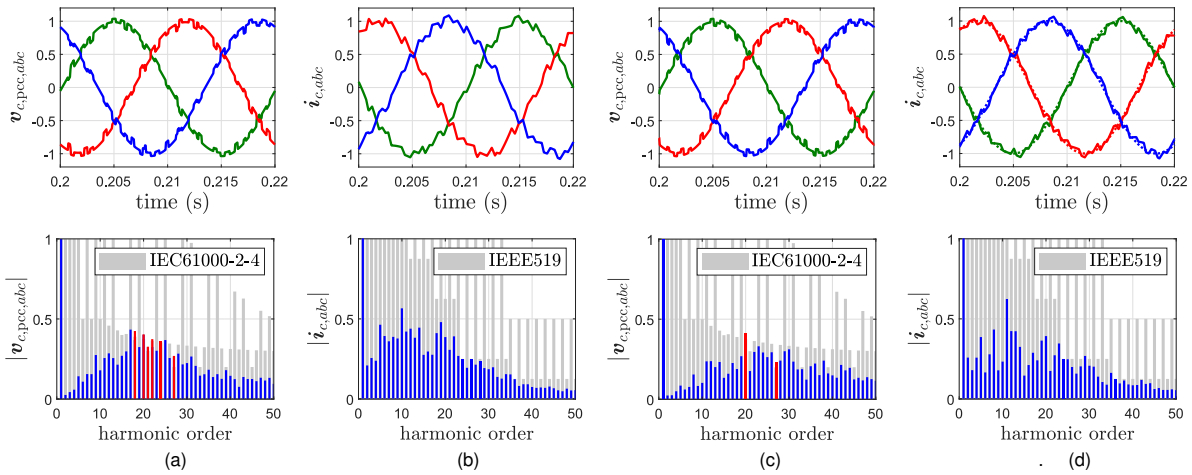


**Fig. 5:** Simulated waveforms of the three-phase voltage and current at the PCC of the AFE converter side, and spectrum analysis superimposed to the grid standards (integer components multiples of $f_g$): IEEE 519 (for $k_{\text{sc}} = 20.64$) and IEC 61000-2-4 (for Class 2). Power FCS-MPC: (a) Three-phase voltages at PCC; (b) Three-phase currents. Current FCS-MPC: (c) Three-phase voltages at PCC; (d) Three-phase currents.The DR side will affects the PCC with deterministic hamronics.

of frequencies. The produced TDDs from the power controller are $I_{c,\text{TDD}} = 5.78\%$ and $V_{c,\text{TDD}} = 5.57\%$, while for the current controller $I_{c,\text{TDD}} = 5.12\%$ and $V_{c,\text{TDD}} = 5.14\%$, respectively. The spectral analysis of the DR side is omitted since already provided in [3].

Given $k_{\text{sc}} = 20.64$, the IEEE 519 standard indicates a maximum $I_{\text{TDD,max}} = 8\%$ with the harmonics limits depicted in Figs. 5(b) and 5(d) as light gray bars. Integer harmonics of $\boldsymbol{i}_{c,abc}(t)$ that meet these limits are shown as blue bars, while harmonics that violate them are depicted as red bars. The same is done in Figs. 5(a) and 5(c) for $\boldsymbol{v}_{c,\text{pcc},abc}(t)$ with the IEC 61000-2-4 standard, which refer to a Class 2 electromagnetic environment. The IEEE 519 requirements are met by both controllers. In particular, the current controller tends to produce harmonic components with lower amplitude from $30\text{th}$ to $40\text{th}$ harmonic orders,—i.e., where the standard limits start to become more stringent—while the power controller produces less harmonic energy beyond the $40\text{th}$ harmonic. Since the current controller directly controls the current—rather than indirectly as the power controller does—a better shaping of the spectrum is achieved by shifting the harmonic energy from lower to higher frequencies, which helps to meet the grid standards. Regarding the IEC 61000-2-4, the power FCS-MPC shows several violations at high-order triplen odd components, while the current FCS-MPC only at the $20\text{th}$ and $27\text{th}$. Note that by using the current controller and changing the horizon $N_p$, an $L$-filter may be enough to meet both standards rather than using more expensive $LCL$-filters, which would be necessary in case of power FCS-MPC.

The influence of the horizon length on the current TDD is investigated while $f_{\text{sw}}$ is kept equal to $450\,\text{Hz}$. As can be seen in Fig. 6, a long horizon with current FCS-MPC results in significant improvements in the current TDD, which reduces from $I_{c,\text{TDD}} \approx 5.8\%$ with $N_p = 1$ to $I_{c\text{TDD}} = 5.1\%$ with $N_p = 12$. Similar reduction can

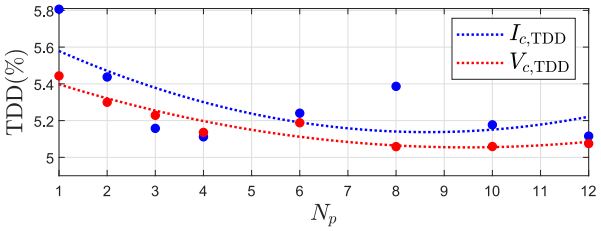


**Fig. 6:** Current and voltage TDD as function of the prediction horizon $N_p$, with $\lambda_u$ adjusted to keep $f_{\text{sw}} \approx 450\,\text{Hz}$. The data points relate to individual simulations, which were approximated using a $2\text{nd}$ degree polynomial.

be observed in the PCC voltage TDD $V_{c,\text{TDD}}$. Hence, it can be concluded that the current control approach is the preferred choice, since it takes advantage of its problem formulation which allows for longer horizons at a moderate computational cost, leading to lower harmonic distortions.

## 5.2 Transient Operations

The transient performances of the proposed algorithms are tested with two step-wise reference changes. For the same $N_p$, $\lambda_q$ and $\lambda_u$ as in Section 5.1, the system response, shown in Figs. 4(a) and 4(b), refers to a real power change from $P_{\text{in2,ref}} = 1$ to $1.5\,\text{p.u.}$; note that in Fig. 4(b) this is translated into a current change along the $d$-component. Fig. 4(c) depicts the voltage sag due to the current absorbed by a train crossing the substation, i.e., from $i_{\text{dc}} = 0.61$ to $0.76\,\text{p.u.}$[6], and its stabilization through power compensation.

Both MPC algorithms show similar tracking performances. In particular, the results in Fig. 4(c) could be achieved by both controllers since it is largely affected by the outer PI controller, which is the same in both control

[6] Note that a substation as the one in this case study is subject to dc-link fluctuations from $3.3$ to $4\,\text{kV}$ during acceleration and braking, due to the train comsumptions [2]. This motivated the proposed transient.

schemes. Note that the reference target for $v_{\mathrm{dc2}}(t)$ is raising during transient because (21) holds, and $v_{\mathrm{dc2}}(t)$ decreases as $v_{\mathrm{dc2}}(t)$ increases. Based on these results, it can be concluded that both steady-state and transient performance of the modular rectifier are good.

# 6 Conclusions

This paper presented a long-horizon direct model predictive approach for a series-connected modular rectifier, including $L$-filters. By appropriately modeling the system dynamics, two control formulations were provided, namely, a power and a current control method. Both optimization problems are incorporating a hard constraint resulting from the inherent controllability limitation of such topology. The effectiveness of the proposed strategy was evaluated through simulations both at steady-state and transient operation. When comparing the ac waveforms at the PCC with the industrial standards, like IEEE 519 and IEC 6000-2-4, it was concluded that the current controller showed a favorable harmonic spectrum as compared with that produced by the power controller. Hence, the proposed current FCS-MPC, solved with sphere decoding, is the preferred choice since it can also achieve longer horizon with a moderate computational effort. Due to the fact that the upgrade of dc rail traction power supply, and its related markets, have not found a clear standardization yet, such control approach seems a promising alternative which may reduce the usage of bulky input filters to meet the standards.

# Acknowledgement

This work is supported by the project “Future Unified DC Railway Electrification System” FUNDRES (Shift2Rail, No.: 881772), funded by H2020.

# References

[1] M. Brenna, F. Foiadelli, and D. Zaninelli, *Electrical Railway Transportation Systems*. Wiley, 2018, p. 622.

[2] A. Clerici, E. Tironi, and F. Castelli-Dezza, “Multiport Converters and ESS on 3-kV DC Railway Lines: Case Study for Braking Energy Savings”, *IEEE Tran. on Industry Applications*, vol. 54, no. 3, pp. 2740–2750, 2018.

[3] M. Rossi, E. Liegmann, P. Karamanakos, F. Castelli-Dezza, and R. Kennel, “Direct model predictive power control of a series-connected modular rectifier”, in *Proc. IEEE Int. Symp. Pred. Control of Elect. Drives and Power Electron.*, 2019, pp. 1–6.

[4] IEEE Std 519-2014, *IEEE recommended practices and requirements for harmonic control in electrical power systems*, 2014.

[5] IEC 61000-2-4, *Electromagnetic compatibility (EMC)—part 2-4: Environment—compatibility levels in industrial plants for low-frequency conducted disturbances*, 2002.

[6] P. Cortés, M. P. Kazmierkowski, R. M. Kennel, D. E. Quevedo, and J. Rodríguez, “Predictive control in power electronics and drives”, *IEEE Trans. Ind. Electron*, vol. 55, no. 12, pp. 4312–4324, 2008.

[7] J. Rodríguez, M. P. Kazmierkowski, J. R. Espinoza, P. Zanchetta, H. Abu-Rub, *et al.*, “State of the art of finite control set model predictive control in power electronics”, *IEEE Trans. Ind. Informat.*, vol. 9, no. 2, pp. 1003–1016, 2013.

[8] P. Cortes, J. Rodriguez, P. Antoniewicz, and M. Kazmierkowski, “Direct Power Control of an AFE Using Predictive Control”, *IEEE Transactions on Power Electronics*, vol. 23, no. 5, pp. 2516–2523, 2008.

[9] D. E. Quevedo, R. P. Aguilera, M. A. Perez, P. Cortes, and R. Lizana, “Model Predictive Control of an AFE Rectifier With Dynamic References”, *IEEE Transactions on Power Electronics*, vol. 27, no. 7, pp. 3128–3136, 2012.

[10] T. Geyer, J. Scoltock, and U. Madawala, “Model Predictive Direct Power Control for Grid-Connected Converters”, in *37th Annual Conference of the IEEE Industrial Electronics Society (IECON)*, Australia, 2011, pp. 1438 –1443.

[11] T. Geyer, P. Karamanakos, and R. Kennel, “On the benefit of long-horizon direct model predictive control for drives with $LC$ filters”, in *Proc. IEEE Energy Convers. Congr. Expo.*, Pittsburgh, PA, 2014, pp. 3520–3527.

[12] P. Karamanakos and T. Geyer, “Guidelines for the design of finite control set model predictive controllers”, *IEEE Trans. Power Electron.*, pp. 1–17, 2020, in press.

[13] T. Geyer and D. E. Quevedo, “Multistep finite control set model predictive control for power electronics”, *IEEE Trans. Power Electron.*, vol. 29, no. 12, pp. 6836–6846, 2014.

[14] N. Mohan, T. M. Undeland, and W. P. Robbins, *Power Electronics: Converters, Applications and Design*, 3rd. Hoboken, NJ: Wiley, 2003.

[15] P. Karamanakos, T. Geyer, and R. Kennel, “On the choice of norm in finite control set model predictive control”, *IEEE Trans. Power Electron.*, vol. 33, no. 8, pp. 7105–7117, 2018.

[16] T. Geyer, *Model predictive control of high power converters and industrial drives*. Hoboken, NJ: Wiley, 2016.

[17] P. Karamanakos, T. Geyer, N. Oikonomou, F. D. Kieferndorf, and S. Manias, “Direct model predictive control: A review of strategies that achieve long prediction intervals for power electronics”, *IEEE Ind. Electron. Mag.*, vol. 8, no. 1, pp. 32–43, 2014.

[18] P. Karamanakos, T. Geyer, and R. Kennel, “Constrained long-horizon direct model predictive control for power electronics”, in *Proc. IEEE Energy Convers. Congr. Expo.*, Milwaukee, WI, 2016, pp. 1–8.

[19] B. Hassibi and H. Vikalo, “On the sphere-decoding algorithm I. Expected complexity”, *IEEE Trans. Signal Proc.*, vol. 53, no. 8, pp. 2806–2818, 2005.

[20] T. Geyer and D. E. Quevedo, “Performance of multistep finite control set model predictive control for power electronics”, *IEEE Trans. Power Electron.*, vol. 30, no. 3, pp. 1633–1644, 2015.

[21] M. Dorfling, H. Mouton, T. Geyer, and P. Karamanakos, “Long-horizon finite-control-set model predictive control with non-recursive sphere decoding on an FPGA”, *IEEE Trans. Power Electron.*, pp. 1–12, 2020, in press.